International Journal of Multiphase Flow 35 (2009) 171–184

Contents lists available at ScienceDirect

International Journal of Multiphase Flow

journal homepage: www.elsevier.com/locate/ijmulflow

Countercurrent gas/liquid flow and mixing: Implications for water disinfection ☆

Timothy A. Bartrand [a], Bakhtier Farouk [b,*], Charles N. Haas [a]

[a] Department of Civil, Architectural and Environmental Engineering, Drexel University, Philadelphia, PA 19104, USA
[b] Department of Mechanical Engineering and Mechanics, Drexel University, 3141 Chestnut Street, Philadelphia, PA 19104, USA

ARTICLE INFO

Article history:
Received 27 October 2006
Received in revised form 27 June 2008
Accepted 11 August 2008
Available online 27 September 2008

Keywords:
Countercurrent
Bubble column
Dispersion
CFD

ABSTRACT

Experimental and numerical results are presented from investigations into the hydrodynamics of a bench scale bubble column reactor. Countercurrent bubble column reactors are most commonly used in water disinfection for effecting mass transfer of ozone to the aqueous phase. In the reactor column used in this study, gas is introduced at the bottom of the column via a spherical diffuser and water is introduced to the top of the column through a manifold packed with glass spheres. Residence time distribution (RTD) studies were conducted for a range of gas flow rates chosen to span the dispersed flow bubble regime. A multiphase computational fluid dynamics (CFD) model was used to simulate the flow in the bubble column and to gain insights into the fluid dynamics of countercurrent flow bubble columns. The CFD model accurately predicted trends in mixing. Use of CFD in bubble column design and scale-up thus may yield better designs than those based on empirical relations.

1. Introduction

Dissolved ozone is employed in water and wastewater treatment for taste and odor control, advanced oxidation processes, pre-treatment for improved flocculation and settling and for disinfection of pathogenic organisms and the control of disinfection by-products (DBPs). Ozone is a stronger disinfectant than chlorine and can inactivate organisms resistant to chlorine (such as *Cryptosporidium parvum*) at doses and times realizable in practical reactors. Ozone has been in use for disinfecting bottled water for more than 30 years because of its effectiveness as a disinfectant and because it leaves no residual or undesirable taste in treated water. Depending upon raw water chemistry, ozone may generate lower concentrations of DBPs than chlorine. However, for waters containing bromide, ozonation of water may result in the production of bromate, a regulated contaminant in the United States and European Union and a known human carcinogen (von Gunten, 2003).

Countercurrent bubble column contactors are the most-frequently used reactors for dissolution of gaseous ozone into the aqueous phase in municipal water and wastewater treatment. In bottled water treatment, in-line ozonation via bubble column reactor and batch ozonation are practiced. The prevalence of ozonation via bubble column reactors arises from their simple design, low energy requirements (excluding the energy required in ozone generation) and their familiarity to the industry and regulatory agencies (Langlais et al., 1991; Rakness et al., 1984). Full-scale contactors typically employ baffled chambers in which ozonated gas is contacted with untreated water in both countercurrent and cocurrent fashion (Cockx et al., 1999; Tang et al., 2005). Design of these reactors is performed using scale-up data collected in pilot-scale bubble contactors, most often right circular cylinders (Haas et al., 1995; Owens et al., 2000). Pilot studies are used to evaluate reactor hydraulics (dispersion), ozone transfer rate for the expected range of gas and liquid flow rates and water chemistry (ozone demand and decay) and to confirm microbial inactivation rates developed in batch studies.

Adequate inactivation of pathogenic organisms occurs by contact with dissolved ozone and requires sustained contact between the organisms and ozone. Liquid phase mixing plays a dual role in contact of organisms with disinfectant; ozone mass transfer rate depends on liquid phase renewal at bubble surfaces and advection of dissolved ozone into the pathogen-laden liquid stream depends on large scale mixing. Although many studies have explored the details of fluid motion in bubble columns with a stagnant liquid phase (Cui and Fan, 2004; Deen et al., 2001; Degaleesan et al., 2001; Delnoij et al., 1999; Ekambara and Joshi, 2003; Forret et al., 2003; Jakobsen, 2001; Joshi et al., 2002; Krishna et al., 1999; Lan et al., 1999; Laín et al., 2002; Mitra-Majumdar, 1997; Mitra-Majumdar et al., 1998; Peplinski and Ducoste, 2002; Pfleger et al., 1999; Sanyal et al., 1999; van Baten and Krishna, 2001), relatively few studies have been carried out for mixing in countercurrent bubble flow systems. Among studies performed on countercurrent bubble column reactors, all have assumed, either implicitly or explicitly, that mixing is uniform in the direction of liquid flow.

In the current study, flow visualization, residence time distribution (RTD) and computational fluid dynamics (CFD) analyses were

☆ Submitted for publication to the International Journal of Multiphase Flows, October, 2006; in revised forms, August 2007, June 2008.

* Corresponding author. Tel.: +1 215 895 2287; fax: +1 216 5 895 1478.
E-mail address: bfarouk@coe.drexel.edu (B. Farouk).

0301-9322/$ - see front matter © 2008 Elsevier Ltd. All rights reserved.
doi:10.1016/j.ijmultiphaseflow.2008.08.004

used in tandem to produce a detailed description of mixing in a laboratory countercurrent bubble column reactor. The use of these tools in tandem provided quantitative data on macro-scale and micro-scale mixing mechanisms in countercurrent flow. The open literature on bubble column flows do not provide adequate details of these processes (Zahradník and Fialová, 1996). Several notable differences differentiate the current study from those of previous researchers:

- The bubble column reactor used in the current study was designed to minimize entrance and exit effects.
- The spatial distribution of mixing in the reactor is described and modeled in detail in the current study.
- The current study utilizes RTD and CFD analyses for estimating axial dispersion.
- In the current study, minor misalignment of the bubble column was included in CFD modeling.

2. Background and past studies

2.1. Geometric parameters and orientation

In pilot studies of bubble columns of differing diameter and with a non-flowing liquid phase, the column diameter influenced mixing due to the dependence of large-scale fluid structure (circulation) on column diameter but did not influence gas phase holdup (Forret et al., 2003; Krishna et al., 1999; Ruzicka et al., 2001). Column height can also influence transition from homogeneous to heterogeneous bubbly flow and dispersion in columns with non-flowing liquid phase, with transition occurring earlier as column height is increased (Ruzicka et al., 2001). Minor vertical misalignment of tall cylindrical bubble columns can drastically change column hydrodynamics; a reactor tilt of only 0.5° resulted in a three order of magnitude difference in dispersion observed in pilot studies of air injected into water in a 2.44 m tall bubble column (Rice and Littlefield, 1987).

In full-scale ozone bubble column reactors, the arrangement of baffles dominates reactor hydrodynamics; gas injection scheme (distribution of gas injection between reactor compartments) plays a less significant role (Do-Quang et al., 2000). The spacing of spargers and their proximity to reactor walls influence reactor hydrodynamics, given the tendency of bubble plumes to migrate toward each other (Freire et al., 2002) or toward reactor walls (Machina et al., 1992).

Using drift flux analysis and experimentation, Hasan et al. (1994) observed that holdup in bubble columns differs significantly for cocurrent and countercurrent modes of operation. For countercurrent operation in the ideal bubbly flow regime, Argo and Cova (1965) determined that gas superficial velocity has a greater influence on dispersion than liquid superficial velocity.

2.2. RTD analyses

RTD studies have been used to gain insights into the complex hydrodynamics of continuous flow reactors and optimize chemical processing operations (Danckwerts, 1953, 1958; Levenspiel and Smith, 1957; Nauman and Buffham, 1983). In environmental engineering, RTD analyses have been used to assess the hydraulics of wetlands (Schmid et al., 2004), aeration processes (Burrows et al., 1999), filtration and disinfection processes (Teefy and Singer, 1990), flocculation processes (Ives and Hoyer, 1998) and chlorine contact chambers (Hart, 1979a,b; Sawyer and King, 1969; Sepp, 1981). Relatively recently, RTD studies have been incorporated into the integrated disinfection design framework (IDDF) (Bellamy et al., 1998; Ducoste et al., 2001), a framework of techniques for modeling and design of potable water disinfection processes.

Tracer data are relatively easy to generate but do not provide detailed information about reactor hydrodynamics; the same tracer response may arise from reactors with significantly different flow patterns. So analysis of tracer data and attempts to relate RTDs to flow phenomena are essential when tracer data are used in scale-up or troubleshooting underperforming reactors.

In tracer studies, the tracer may be introduced as a pulse or as a step function. In the current study step tracer experiments were used. Tracer experiment methodology is described below. If plug flow were encountered in the reactor and a step tracer were introduced at the reactor intake, the tracer response at the discharge would be a step function with the tracer concentration at the discharge equal to the feed tracer concentration after one theoretical hydraulic residence time. For realistic bubble column flows, uneven distribution of phases and the turbulence present in the bubble wakes result in spreading of the tracer response, with some tracer appearing at the discharge before the theoretical hydraulic residence time (e.g., due to uneven distribution of phases) and tracer concentration less than feed concentration after the theoretical hydraulic residence time (e.g., due to backmixing of the tracer by the bubble plume). The spread of the tracer curve (the deviation of the tracer curve from plug flow) provides a measure of the axial dispersion of the reactor. RTD analysis is used to estimate axial dispersion from experimental tracer data.

In the current study, RTD analysis entailed:

- *Tracer studies*. A conservative tracer, NaCl, was introduced to the reactor feed as a step function and its concentration was measured 6 cm downstream of the reactor discharge.
- *Development of an experimental residence time distribution*. Tracer data were processed and an experimental cumulative distribution function (F) of tracer residence times was produced. F is the normalized tracer concentration (with the background tracer concentration subtracted) and it is given by

$$F = \frac{C_{\text{Tracer}} - C_{\text{Background}}}{C_{\text{Feed}} - C_{\text{Background}}} \tag{1}$$

- *Determination of a best fit residence time distribution model*. Cumulative distribution functions (CDFs) that approximate the solution to ideal reactor tracer response are fit to the experimental residence time distribution. Parameters of the CDFs that provide the best fit to the experimental residence time distribution were determined through non-linear regression.

Several prior researchers have used tracer studies to explore mixing in countercurrent flow bubble columns. Results from these studies are compared with those generated in the current study. Relations for the dispersion number, D, and axial dispersion, E_L, drawn from prior studies of countercurrent flow bubble column mixing are presented in Table 1. Significant findings of prior RTD analyses are highlighted below. In this work, *dispersion number*, D, is the ratio of dispersive to advective transport, as defined in the following equation

$$D = \frac{E_L}{u_L H} \tag{2}$$

In Eq. (2), u_L is liquid phase superficial speed (volumetric flow rate divided by column cross sectional area) and H is bubble column height.

Mariñas et al. (1993) calculated dispersion number for a range of gas and liquid flow rates for a 17.6 cm diameter bubble column reactor. Pulse tracer studies were performed with the reactor un-

Table 1
Countercurrent flow dispersion relations

Relation	Study
$E_L \propto \frac{u_g^2 d_c}{\upsilon_b}$	Bischoff and Phillips (1966)[a]
$D^{-1} = \frac{(2u_G+\upsilon_b)d_c}{E_L} = 3.0 \pm 0.3$	Reith et al. (1968)[b]
$D^{-1} = \frac{u_G H}{0.35(u_G g)^{1/3} d_c^{4/3}}$	Baird and Rice (1975)[c]
$D = \frac{4.88}{H}\left[0.00185 + 9.7\frac{u_G^{1/2}}{u_L^{5/3}}\left(\frac{\nu_L}{d_b}\right)^{7/6}\right]$	Kim et al. (2002)[d]

[a] Based on analysis of data from numerous small diameter cocurruent, countercurrent and non-flowing liquid phase bubble columns. Only valid in the ideal bubbly flow regime.

[b] Based on experimental data taken in 5 and 14 cm cocurrent and countercurrent bubble columns in which air was sparged into tap water. The term $2u_g + \upsilon_b$ is the relative velocity between phases.

[c] Developed for co- and countercurrent flow in a 15 cm circular bubble column. Units of H is in m and all other units must be dimensionally consistent.

[d] Developed using dispersion data collected from several studies and under the assumption of isotropic turbulence and turbulent energy dissipation rate equal to $(u_g g)$.

packed, undergoing countercurrent flow and for the reactor packed with plastic saddles and undergoing cocurrent flow. Dispersion number was estimated via method of moments. Countercurrent experiments were performed with two different spargers and at a range of water depths. The authors found that:

- For the unpacked column with a coarse diffuser, the dispersion number is not strongly influenced by water flow rate and is not strongly influenced by water depth as long as the ratio of the water depth to column diameter is greater than 11.
- The dependence of dispersion on water depth for water depth to column diameter ratio less than 11 was attributed to the "mixing zone" present near the diffuser. This mixing zone gives rise to short circuiting in the liquid phase and backmixing of the liquid stream by the bubble plume.

Prior studies (Drahos et al., 1992; Rice and Littlefield, 1987; Zahradník and Fialová, 1996), demonstrated that slight vertical misalignments resulted in profound changes in the dispersion number. Drahos et al. (1992) attributed the profound differences arising from misalignment to the development of large, asymmetric recirculating regions, especially near the reactor liquid intake and discharge.

2.3. Review of prior numerical studies

Numerous CFD studies have been made of bubble columns with non-flowing liquid phase. These studies have explored the submodels best suited for reproducing bubble column hydrodynamics in general and momentum exchange between phases and bubble break-up and coalescence in specific. Significant differences between published studies are treatment of the dispersed phase, viz. Eulerian (Olmos et al., 2003; Pan et al., 2000; Pfleger et al., 1999; van Baten and Krishna, 2001) or Lagrangian (Lan et al., 1999, 2002), distribution of bubble diameters, viz. monodisperse (Pfleger et al., 1999) two size groups (van Baten and Krishna, 2001) or a distribution of bubble diameters (Olmos et al., 2003) and bubble drag model. Based on the reported success and relative simplicity of the Eulerian–Eulerian approach and use of a two-equation turbulence model for the liquid phase, this approach is adopted for the current study.

A number of researchers have performed CFD studies of ozone bubble contactors (Brouckaert and Buckley, 1999; Cockx et al., 1999; Henry and Freeman, 1995; Murrer et al., 1995; Ta and Hague, 2004), providing insights into the hydrodynamics and optimal design of ozone contactors for water treatment. Among the studies in which the gas phase was modeled as a separate fluid, all the studies cited used the Eulerian–Eulerian approach. In the only study in which details of interphase momentum transfer were presented, Cockx modeled the gas phase as monodisperse with a bubble diameter of 3 mm and a uniform drag coefficient equal to 1.0. The foregoing citations indicate the potential for using CFD as a design and analysis tool for ozone contactors and the importance of validation and discussion of submodels.

3. Methods

3.1. Experimental methods

Tracer studies were performed in the countercurrent flow bubble column illustrated in Figs. 1 and 2. The reactor is a glass cylinder with an internal diameter of 15.3 cm and height of 1.83 m. Breathing quality air is introduced at the bottom of the column via a 2.5 cm spherical fine pore diffuser. Water enters the column via two ports at the bottom of the collar that encloses the top of the column. The distance between the tracer stock solution and the column entrance was measured to be 0.7 m. For the tracer solution flow rate used in the present study, the time required for the tracer to reach the column after column feed was switched to tracer from tap water was approximately 4 s. Accordingly, tracer sample times were adjusted by 4 s to reflect this lag. The space between the column and collar is packed with 7 mm glass beads to diffuse the momentum of the influent water. Water flows out of the column through four symmetric ports located approximately 3 cm below the bottom of the diffuser. The volume between the bottom of the diffuser and the discharge ports is also packed with glass beads to promote uniform flow. The sparger assembly consists of a short tube threaded into a fitting machined in the center of the column base.

To align the column vertically, the base upon which the column sits was leveled. The legs supporting the column are threaded rods and the column base is supported by nuts threaded onto the rods. The column base was leveled via adjustment of the nuts.

Step tracer studies (dissolved NaCl tracer) were performed at a liquid flow rate of 6.6 L/min and at gas flow rates of 0, 0.5, 1, 2, 3 and 3.5 L/min. This liquid flow rate provided a theoretical hydraulic residence time (θ_H, defined as the column volume divided by the liquid volumetric flow rate) of 296 s (4.93 min). Gas flow was observed to be in the ideal bubbly regime at all gas flow rates, though, as will be described later, the liquid phase flowfield and distribution of bubbles in the column changed significantly over the range of gas flow rates. Salt tracer concentration was measured as conductivity using a dip cell conductivity meter (VWR Model 2052). The conductivity meter automatically corrects for changes in temperature and measures conductivity (electrical) to ±0.001 mS. In all experiments, the conductivity ranged from 0.304 to 1.884 mS.

During tracer studies, samples were taken at 15 s intervals from a port approximately 6 cm downstream of the column's water discharge ports. The sample port is shown in Fig. 1. Prior to tracer studies the column was operated at the chosen water and gas flow rates for at least three theoretical residence times. During tracer experiments, tracer was introduced to the column via step feed for three theoretical residence times, then tracer feed was replaced with tap water and tracer was washed out for at least three theoretical residence times.

Two flow visualization studies were performed. In the first, the salt tracer was replaced with an indigo dye (used for colorimetric determination of ozone concentration (Bader and Hoigné, 1981)) and the progress of the step feed of dye was recorded in digital photographs. Elsewhere, the color of the dye has been shown to be proportional to the dye concentration (Bartrand, 2006). Concentrated dye and tap water were mixed via a static mixer located

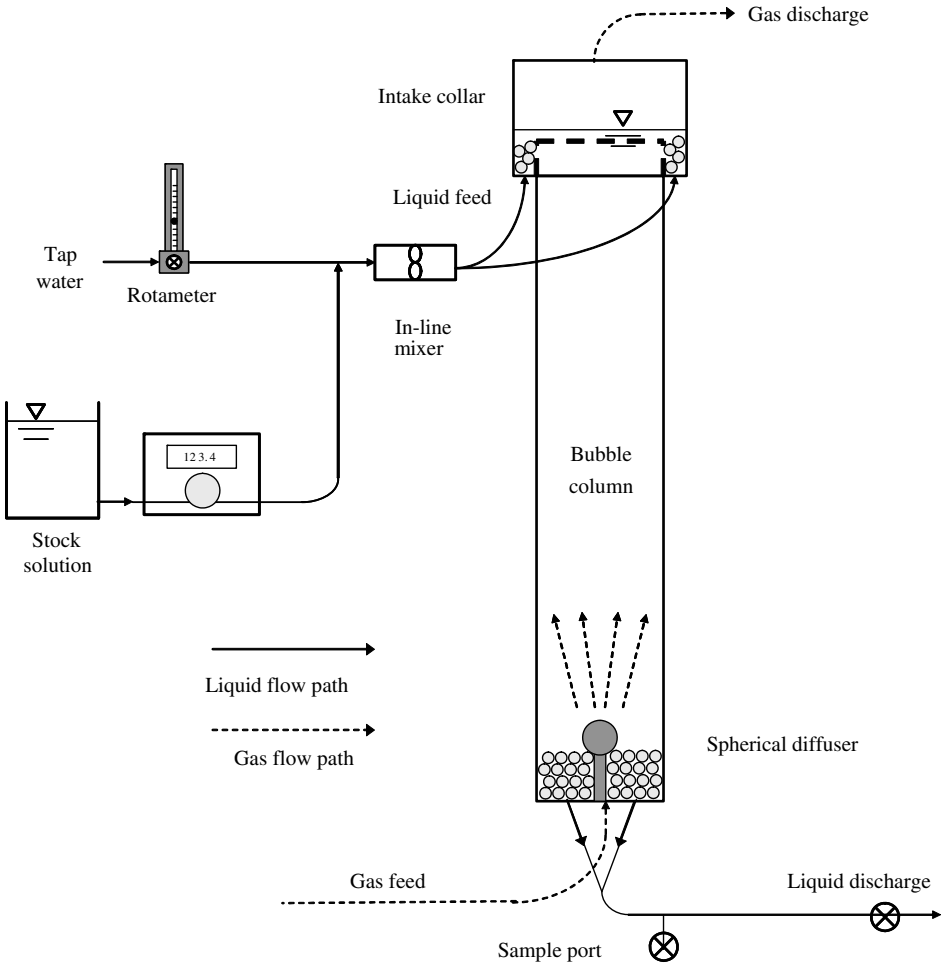

Fig. 1. Laboratory reactor schematic. Tracer sample port indicated at the bottom of the schematic diagram.

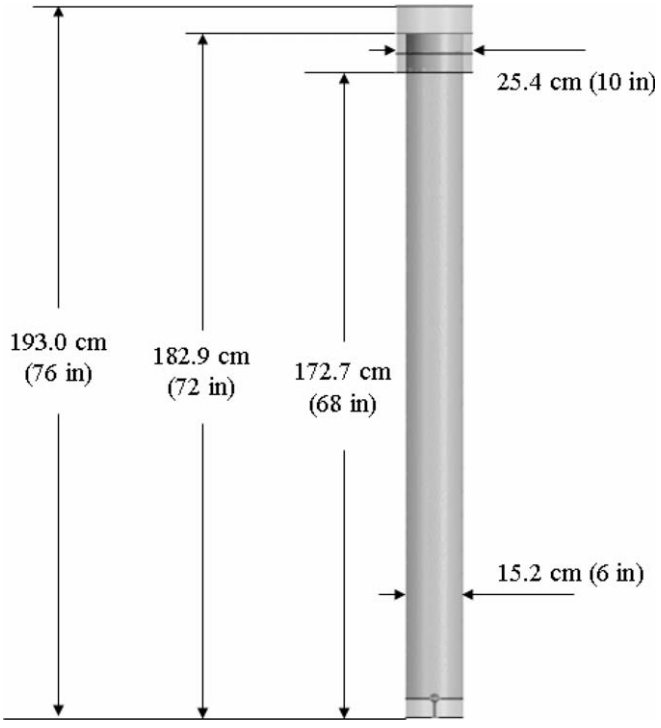

Fig. 2. Bubble column reactor scale drawing.

approximately 20 cm upstream of the column water intake. In a second visualization study, an indigo dye solution was used as the liquid feed of the bubble column and the gas feed was a mixture of air and ozone (approximately 2.5% ozone by volume). Dissolved ozone rapidly decolors indigo dye, so disappearance of dye indicates ozone mass transfer from the gas to the liquid phase. Distribution of the indigo dye in the reactor is then indicative of distribution of ozone mass transfer from the bubbles to the liquid phase.

3.2. Mathematical model

A two-phase model (Eulerian–Eulerian) is employed for the numerical solution of the gas/liquid flowfields and phase distributions. In this model, the phases are modeled as uniformly mixed within a given mesh element and the volume occupied by phase α in that mesh element is denoted ϕ_α. In the current two phase study, ϕ_L is liquid volume fraction, ϕ_G is gas volume fraction and $\phi_G + \phi_L = 1.0$. The Eulerian–Eulerian model offers a less computationally intensive framework for modeling two-phase flow than Eulerian–Lagrangian approaches. Though the Eulerian–Lagrangian approach may provide more precise representation of bubbly flows in the dispersed flow range, it is the authors' estimation that the Eulerian–Eulerian approach is better suited to simulation of full-scale contactors when the objective of the simulation is prediction of gross phase distribution and mixing, as required in design or improvement of ozone contactors. Successful use of the Eulerian–Eulerian framework in simulation of low void fraction bubbly flow by Lopez de Bertodano et al. (2004) indicates that this approach is

viable and that accurate characterization of the turbulent dispersion force yielded agreement between predicted and measured void fractions. Consistent with the authors' goal to extend the analyses to full-scale contactors, the Eulerian–Eulerian approach was selected and assessed in the current study.

Assuming no source terms for the liquid and gas phases and no mass transfer between phases due to phase change, the two-phase model continuity and momentum equations are

$$\frac{\partial}{\partial t}(\phi_\alpha \rho_\alpha) + \nabla \bullet (\phi_\alpha \rho_\alpha \vec{V}_\alpha) = 0 \tag{3}$$

and

$$\frac{\partial}{\partial t}(\phi_\alpha \rho_\alpha \vec{V}_\alpha) + \nabla \bullet [\phi_\alpha (\rho_\alpha \vec{V}_\alpha \times \vec{V}_\alpha)] = -\phi_\alpha \nabla P_\alpha + \nabla \bullet \{\phi_\alpha \mu_\alpha [\nabla \vec{V}_\alpha + (\nabla \vec{V}_\alpha)^T]\} + \vec{F}_\alpha \tag{4}$$

where ρ_α, V_α, P_α and μ_α are the density, velocity, pressure and viscosity of phase α, respectively, and F_α is the interfacial force acting on phase α due to the presence of the other phase. For the current problem, the only interfacial forces of significance are drag force and interphase turbulent dispersion force and

$$\vec{F}_\alpha = \vec{F}^D_\alpha + \vec{F}^T_\alpha \tag{5}$$

where $\vec{F}^D_\alpha$ is the interfacial force due to drag and $\vec{F}^T_\alpha$ is interfacial force due to turbulent dispersion.

The drag component of the interfacial force term is given as

$$\vec{F}^D_\alpha = \frac{C_D}{8} A_{\alpha\beta} \rho_\alpha (\vec{V}_\beta - \vec{V}_\alpha) \mid \vec{V}_\beta - \vec{V}_\alpha \mid \tag{6}$$

where C_D is drag coefficient, $A_{\alpha\beta}$ is the net interfacial area between the phases and $\vec{V}_\beta$ and $\vec{V}_\alpha$ are the velocities of phases α and β. The Grace relation was chosen for drag coefficient because bubbles were observed to be elliptical and dispersed. The drag coefficient (Clift et al., 1978) is

$$C_D = \frac{4}{3} \frac{g d_B}{U_T^2} \frac{\Delta\rho}{\rho_L} \tag{7}$$

where g is gravitational acceleration, d_B is mean bubble diameter, $\Delta\rho$ is the difference in density between the phases, ρ_L is liquid phase density and U_T is bubble terminal rise velocity, given by

$$U_T = \frac{\mu_L}{\rho_L d_B} \Lambda^{-0.149} (J - 0.857) \tag{8}$$

In the terminal velocity expression, Λ is the Morton number (a fluid property) given by

$$\Lambda = \frac{\mu_L^4 g \Delta\rho}{\rho_L^2 \sigma^3} \tag{9}$$

where σ is surface tension and J is given by

$$J = \begin{cases} 0.94 B^{0.751} & 2 < B \leqslant 59.3 \\ 3.42 B^{0.441} & B > 59.3 \end{cases} \tag{10}$$

In Eq. (10), B is given by

$$B = \frac{4}{3} Eo \Lambda^{-0.149} \left(\frac{\mu_L}{\mu_{ref}}\right)^{-0.14} \tag{11}$$

and Eo is the Eötvös number, given by

$$\mathrm{Eo} = \frac{g \Delta\rho d_B^2}{\sigma} \tag{12}$$

Turbulent dispersion force is given by

$$\vec{F}^T_\alpha = C_{TD} C_d \frac{\nu_{t,L}}{\sigma_{t,L}} \left(\frac{\nabla \phi_G}{\phi_G} - \frac{\nabla \phi_L}{\phi_L}\right) \tag{13}$$

where C_{TD} is an empirical constant (taken to be 1.0 in the absence of data for turbulent dispersion force in countercurrent flow), C_d is drag coefficient (described above), $\nu_{t,L}$ is turbulent viscosity, $\sigma_{t,L}$ is liquid turbulent Schmidt number (taken to be 0.9) and ϕ_G and ϕ_L are the gas and liquid phase volume fractions, respectively.

Virtual mass force and lift force were neglected because they are presumed much smaller than drag, buoyancy and turbulent dispersion forces and because, given the data available, there is no rational basis for determining the virtual mass and lift force coefficients. A brief justification for neglecting these forces follows. As suggested by Joshi (2001), for bubble columns of diameter >0.15 cm, the role of the added mass term is negligible. In the current work, it is expected that errors associated with representing the bubble plume as monodisperse are much greater than those associated with the virtual mass model.

Although lift force may influence bubble plume spread, specific data were lacking for rational choice of a lift coefficient for deformable bubbles within a coherent bubble stream in countercurrent flow. The value for lift coefficient used most often in other studies of bubbles in shear flows is 0.5. This value was derived for lift experienced by a single spherical bubble rising in a shear flow. Values for measured lift coefficient vary significantly ($-0.07 < C_L < 0.28$), as noted by Lopez de Bertodano et al. (2004) for bubbly jets. Additionally, Lopez de Bertodano noted that in CFD simulations of bubbly flows using an Eulerian–Eulerian framework, for the lift coefficient in the range $0 < C_L < 0.288$, predicted flowfields for bubbly jets were insensitive to choice of lift coefficient. This result is consistent with the experimental findings of Sanada et al. (2005), who observed and modeled a "bubble chain force" for a chain of coherent bubbles. If the majority of bubbles are rising within a coherent structure, the shear exerted on the bubbles will be low and the bubble chain force will be of much greater importance than the lift force. A future study could test this hypothesis for a countercurrent flow bubble column configuration and for a range of gas and liquid flow rates. The two-equation κ–ω turbulence model was chosen because, in 2D steady simulations (not shown) its predicted gas-phase distribution and average turbulent kinetic energy in the bubble column were very close to those predicted with the more-familiar κ–ε model and because in transient simulations the CFD model employing the κ–ω converged to the target residual faster than models employing the κ–ε model. The κ–ω turbulence model for the continuous (liquid) phase is

$$\frac{\partial}{\partial t}(\phi_L \rho_L \kappa_L) + \nabla \bullet \left\{\phi_L \left[\rho_L \vec{U}_L \kappa_L - \left(\mu + \frac{\mu_{t,L}}{\sigma_k}\right) \nabla k_L\right]\right\} = \phi_L (-P_{t,L} + \beta' \rho_L \kappa \omega) \tag{14}$$

$$\frac{\partial}{\partial t}(\phi_L \omega) + \nabla \bullet \left[\phi_L \rho_L \vec{U}_L \omega - \left(\mu + \frac{\mu_{t,L}}{\sigma_\omega}\right) \nabla \omega\right] = \phi_L \left(\lambda \frac{\omega}{\kappa} P_{t,L} - \beta \rho_L \omega^2\right) \tag{15}$$

In Eqs. (14) and (15), κ is the turbulent kinetic energy, ω is the characteristic turbulence frequency, $\mu_{t,L}$ is the liquid phase turbulent viscosity and the constants β, β', σ_k, σ_ω and λ are 0.075, 0.09, 2, 2 and 5/9, respectively. The liquid phase turbulent viscosity is modeled using the Sato particle enhanced turbulence model (Sato and Sekoguchi, 1975), given in the following equation

$$\mu_{t,L} = \mu_{t,s} + \mu_{t,p} \tag{16}$$

where $\mu_{t,s}$ is the conventional shear-induced turbulent viscosity and $\mu_{t,p}$ is a particle induced component of turbulent viscosity given by

$$\mu_{t,p} = C_{\mu,p} \rho_L \phi_g d_b \mid \vec{U}_G - \vec{U}_L \mid \tag{17}$$

and $C_{\mu,p}$ is given a value of 0.6. The term $P_{t,L}$ in Eqs. (14) and (15) is the turbulence production due to viscous forces, calculated as

$$P_{t,L} = \mu_{t,L}\nabla\vec{U} \bullet (\nabla\vec{U} + \nabla\vec{U}^T) - \frac{2}{3}\nabla \bullet \vec{U}(3\mu_{t,L}\nabla \bullet \vec{U} + \rho_L\kappa) \quad (18)$$

The dispersed (gas) phase turbulence is modeled using a zero equation model in which gas turbulent viscosity is proportional to liquid phase turbulent viscosity:

$$\mu_{t,G} = \frac{\rho_G}{\rho_L}\frac{\mu_{t,L}}{\sigma_{t,g}} \quad (19)$$

where $\sigma_{t,g}$ is a turbulent Prandtl number relating the dispersed phase kinematic eddy viscosity to the continuous phase kinematic eddy viscosity. In calculations, $\sigma_{t,g}$ was assumed to equal 1.0.

The governing equation for transport of a conservative scalar quantity (tracer) in the continuous (liquid) phase is given as

$$\frac{\partial}{\partial t}(\phi_L C_T) + \nabla \bullet (\phi_L C_T \vec{U}_L) - \nabla \bullet \left[\phi_L\left(D_{T,L} + \frac{\nu_T}{Sc_T}\right)\nabla C_T\right] \quad (20)$$

where C_T is volumetric concentration of the tracer, $D_{T,L}$ is diffusivity of the tracer in the liquid phase and Sc_T is turbulent Schmidt number. Because there is no mass transfer of the tracer to the dispersed phase, there is no scalar transport equation for the dispersed phase.

Dirichlet inlet boundaries were specified for water (at the top) and air (at the bottom). A degassing boundary condition for the gas (no slip for the liquid phase, sink term for the gas phase) was specified at the top of the reactor. In the laboratory reactor the top of the reactor is a free surface and gas leaves the water at the free surface and flows through a sealed plenum and escapes the plenum at a port located in the center of the plenum top. Four pressure boundaries, located in the bottom of the column, make up the water discharge boundary. In the laboratory reactor, the region between the sparger and water discharge is packed with 7 mm glass beads. This volume is simulated in CFD as a porous volume with transmissivity of 0.01 cm^2. The transmissivity was estimated using the Karman–Cozeny relation.

Simulations were started as steady state and results from steady simulations were used as initial conditions for transient simulations. It was found that the following initial conditions yielded a relatively fast (within 500 iterations) convergence to an rms residual of 1×10^{-4} for all variables:

- Uniform gas velocity equal to the predicted single bubble terminal rise velocity.
- Uniform downward liquid velocity equal to the water volumetric flow rate divided by the reactor cross sectional area.
- Small gas volume fraction, uniform throughout the reactor.

3.3. Numerical model

The governing equations described in the earlier sections were solved numerically for specified initial and boundary conditions with the commercial finite volume CFD package CFX (ANSYS, Inc., 2004) on a three-dimensional unstructured mesh. Mesh density was chosen based on a grid resolution study and generated to provide high resolution at column walls and near the diffuser. To assess the grid resolution, gas volume fraction along the column diameter at about 0.4 m from the bottom was calculated at three mesh densities (coarse, medium and fine). The coarse, medium and fine density grids had 140,000, 372,000 and 712,000 tetrahedral elements, respectively. In grid resolution studies the gas and liquid flow rates were 2 and 6.6 L/min, respectively. Results from the grid resolution study are presented in Fig. 3. The points shown in Fig. 3 show volume fraction in a "cut" line of the mesh; the points shown in the plot are the points at which the line cuts a tetrahedral element side. When the line passes near the vertex of a tetrahedron, a cluster of several points occurs on the cut line. Data

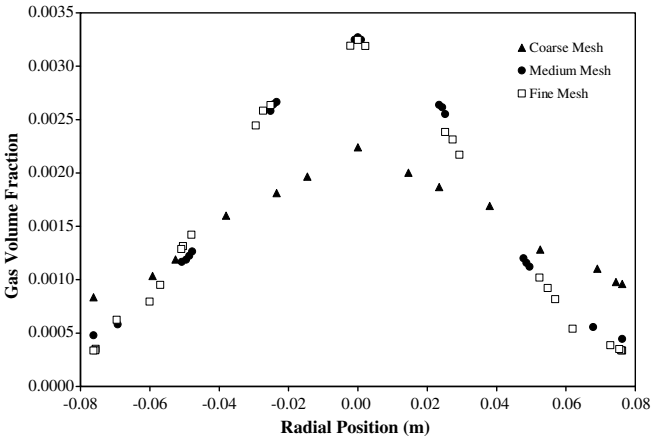

Fig. 3. Predicted gas volume fraction (ϕ_g) profiles for different mesh sizes. Results were generated for gas and liquid flow rates of 2.0 and 6.6 L/min, respectively.

were presented in this way (rather than interpolating to find volume fraction value at regular intervals) to better display the grid spacing for the three meshes. Because differences in the gas fraction profile were minor between the medium and fine meshes, the mesh used in the present study is a refinement of the medium density mesh. Prism elements were added to the medium mesh at the column walls and the grid was refined locally in the vicinity of the sparger, water intake and the top of the column (where water enters the column from the intake section). The resulting grid has a total of 470,000 tetrahedral and prismatic elements.

A second-order upwind transient scheme with relatively small time steps (0.05 s) was required to achieve convergence to an RMS residual of 1×10^{-5} within 10 iterations per time step. To produce representative "quasi-steady" results, calculations were performed for approximately 10 s of simulation time, after which variations in bubble plume shape became minor and bubble plume was seen to rotate in the column, though not with a fixed period.

3.4. Model validation

Based on the observations of Rice and Littlefield (1987) and observations in the laboratory, it was noted that minor misalignments of the column (of less than 0.5° off vertical) or its components (e.g., sparger locations) can drastically change gas and liquid flow and mixing. Despite efforts at leveling the column, locating the diffuser in the column center and ensuring even flow through inlet and discharge ports, it was surmised that perfect alignment of the column was unlikely. So the CFD model included a slight (0.25°) vertical tilt. In the absence of this tilt, CFD predicted a perfectly symmetric bubble plume. When the tilt was included the plume exhibited the asymmetric plume rise observed in bubble column experiments. Specifically, the plume tended to migrate toward the column wall and spiral as it ascended.

The countercurrent flow model was validated using tracer data (described below). Two "virtual tracer" studies – one with single phase flow and one with countercurrent two phase flow – were performed using the CFD model describe above. In the virtual tracer studies, a non-reactive, conservative tracer was introduced as a step feed in the liquid phase at time 0 s and the concentration of the tracer at the reactor discharge was calculated at regular time intervals. For the single-phase virtual tracer study, the liquid flow rate was 6.6 L/min. For the two-phase countercurrent virtual tracer study, gas flow rate and liquid flow rate were 2 and 6.6 L/min, respectively. These gas and liquid flow rates correspond to superficial velocities of 0.17 cm/s for the gas phase and 0.57 cm/s for the liquid phase. Plots showing normalized experimental tracer

concentration (F) and virtual tracer normalized concentration versus normalized time (t/t_H) are presented in Figs. 4 and 5 (single phase) (countercurrent). The numerical results curves in Figs. 4 and 5 are based on transient output from the CFD models taken at 1 s intervals. The definition of normalized tracer concentration is given in Eq. (1) (repeated below).

$$F = \frac{C_{\text{Tracxer}} - C_{\text{Background}}}{C_{\text{Feed}} - C_{\text{Background}}} \quad (1)$$

In both cases, the CFD model faithfully reproduced measured residence time distribution data, though it predicts a slightly earlier breakthrough than that experimentally observed. The agreement between observed and predicted RTDs is considered excellent given the complexity of the flow and the use of a two-equation turbulence model. For the two-phase virtual tracer study, CFD predictions are not monotonic because flow in the bottom of the reactor is unsteady, with the bubble plume turning about the reactor centerline. This behavior is not seen in the experimental data because they are taken at longer time intervals and because samples required approximately 5 s to draw, resulting in an averaging of the tracer concentration. Similar behavior was observed in comparison of a virtual tracer study to experimental data from a single phase serpentine reactor (Santoro et al., 2005). The single-phase virtual tracer concentration did not exhibit these fluctuations.

4. Results

Experimental and numerical studies performed are summarized in Table 2. As described above, tracer studies entailed introduction of a step function of sodium chloride tracer at the reactor inlet and monitoring the conductivity of water at the reactor discharge. For the conductivity meter used in this study, conductivity is a linear function of salt concentration over the concentration range used. Tracer studies generated data for calculation of the dispersion number and characterizing dispersion. Tracer studies were performed at a single liquid flow rate (6.6 L/min) and a range of gas flow rates chosen to span the ideal bubbly flow regime.

In flow visualization studies, rather than a salt tracer, a non-reactive dye was introduced to the reactor as a step function. Flow visualization studies were performed at two gas flow rates (0.4 and 0.7 L/min) and liquid flow rates of 6.6, 9.0 and 12.0 L/min. These flow rates correspond to superficial velocities of 0.034 and 0.060 cm/s for the gas phase and 0.57, 0.77 and 1.03 cm/s for the liquid phase. Flow visualization studies showed phenomena related to early breakthrough of tracer.

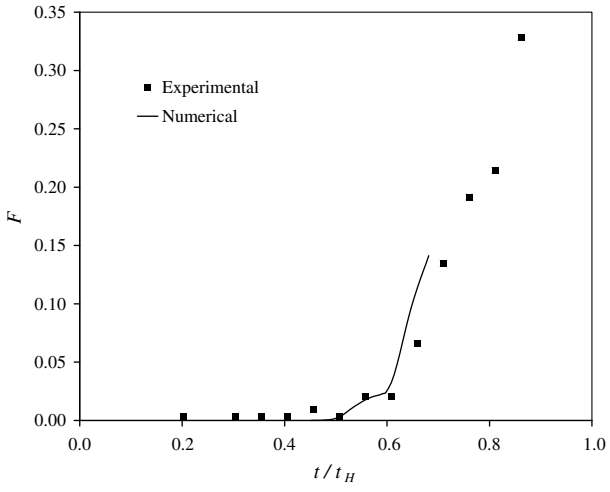

Fig. 4. Normalized experimental and computational tracer concentration (F) versus normalized time for single-phase operation, Q_L = 6.6 L/min.

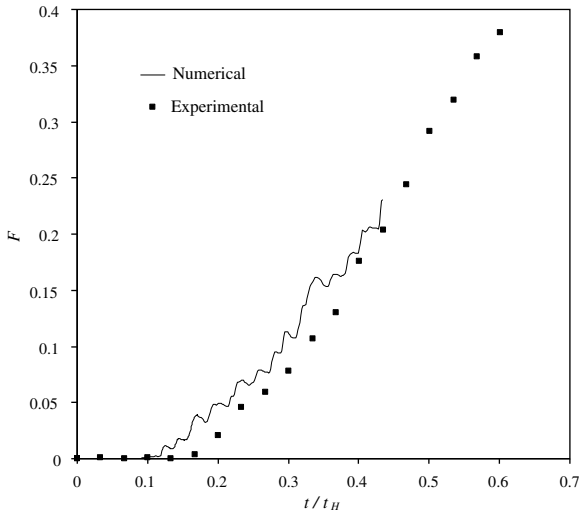

Fig. 5. Normalized experimental and computational tracer concentration (F) versus normalized time for two-phase operation, Q_L = 6.6 L/min and Q_G = 2.0 L/min.

4.1. Bubble plume behavior and flow visualization

As gas flow rate was increased, the behavior of the bubble plume changed significantly, though no increase in bubble breakup or collision was observed. At a low gas flow rate (0.4 L/min) and a liquid flow rate of 6.6 L/min, the plume rises vertically and increases in diameter with height, as shown in Fig. 6a. Analysis of high-resolution digital images indicates bubbles range in shape from nearly spherical to oblate and bubbles tend to ascend in a spiral or zigzag path. At a higher gas flow rate (2.5 L/min), the bubble plume rotates while rising, tending to migrate away from the column centerline and toward the wall as shown in Fig. 6b. At some distance above the sparger (typically between 0.6 and 1 m), the plume expands to fill the entire column. Images similar to those seen in Fig. 6, but including the entire height of the column below the intake region, were analyzed via the image analysis software ImageJ (Rasband, 2007) to determine mean bubble diameter. The particle capture function of the software was able to identify and measure nearly all the bubbles in images when image resolution was high (8 mega-pixels) and when flash photography was employed. Images were thresholded and bubble diameter was estimated based on the ratio of the bubble area to circumference. For gas flow rates at and above 0.7 L/min, the average bubble diameter varied around 2 mm and this value was used for bubble diameter in CFD calculations.

Flow visualization at a water flow rate of 6.6 L/min and a gas flow rate of 2.0 L/min is shown in Fig. 7. The individual frames show the progress of the dye at 30 s, 1.0 min, 1 min 30 s and 2 min after the start of dye injection. Digital image processing was used to remove variations in image color caused by uneven illumination. The black mark seen at approximately one third the reactor's height is the glass manufacturer's mark.

As with salt tracer studies, in flow visualization studies the reactor was operated at steady state for four theoretical hydraulic residence times prior to the introduction of the non-reactive dye (dilute solution of buffered sodium indigo trisulfonate) to the reactor. The dye was fed at a steady rate and concentration for four theoretical hydraulic residence times. The color (darkness) of the image is proportional to the concentration of the dye. The linear relationship between image color and dye concentration was

Table 2
Flow rates considered for the present experimental and numerical studies

Study	Liquid flow rate(s) (L/min)	Gas flow rate (s) (L/min)
Flow visualization	6.6, 10.5, 13.5	0.4, 0.7
Experimental tracer	6.6	0, 0.5, 1.0, 1.5, 2.0, 2.2, 2.4, 3.0, 3.5
CFD studies	6.6, 13.5	0.4, 1.0, 1.5, 2.0, 2.5

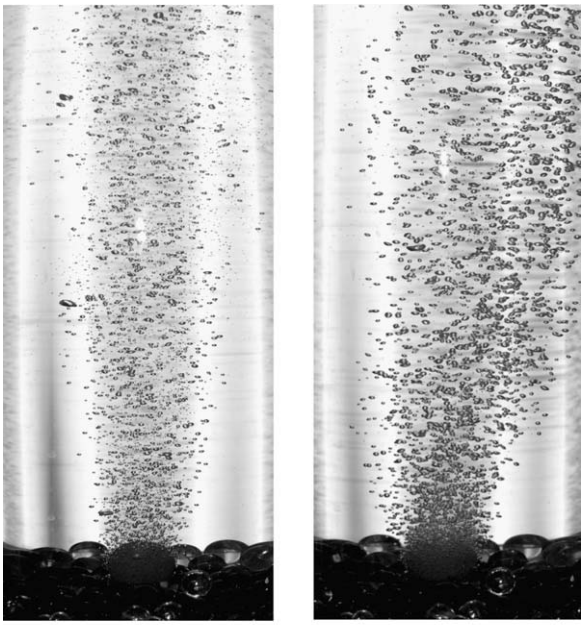

Fig. 6. Photographs of bubble plume shapes. Gas and liquid flow rates in (a) are 0.4 and 6.6 L/min. Gas and liquid flow rates in (b) are 2.4 and 6.6 L/min.

ascertained through analysis of digital images of the reactor filled with uniform solution of dye at seven dilutions.

The liquid phase does not exhibit plug flow behavior; dye proceeds unevenly in the column, tending to flow faster near the column wall. Preferential flow of the dye near the column wall is seen in Fig. 7a–c. As the dye plume proceeds down the column, dye is entrained into the bubble plume (in the center of the column) and back-mixes with the down-flowing stream. This is seen in Fig. 7d. In that frame the front of the dye plume is better mixed than in the prior three frames. Based on these observations, one can expect early tracer breakthrough (due to the rapid progress of the dye near the column wall), and a long tail on the residence time distribution arising from backmixing of the tracer into the bubble plume.

4.2. Residence time distribution analysis

Experimental "*F*" curves corresponding to a liquid flow rate of 6.6 L/min and gas flow rates ranging from 0 to 3 L/min are presented in Figs. 8 and 9. Fig. 8 shows tracer curves for two theoretical residence times and Fig. 9 shows the same data on a scale that emphasizes the early portion of the residence time distribution. The parameters θ and F are the normalized time (t/t_H) and the normalized concentration, defined above in Eq. (1).

The early portions of the *F* curves in Figs. 8 and 9 indicate that increased gas flow rates promote earlier breakthrough. Experimental t_5, t_{10} and t_{20} are shown for $0 < Q_g < 3.0$ L/min in Fig. 10. The times t_5, t_{10} and t_{20} are the times at which 5%, 10% and 20% of the tracer has exited the reactor. In analysis of water treatment processes, the time at which tracer initially appears at the reactor discharge and t_{10} are used in characterization of reactor mixing and, in the case of t_{10}, for regulatory compliance. Fig. 10 shows the relative insensitivity of the early portion of the tracer curve to gas flow rate in the range $0.5 < Q_g < 2.0$ L/min. It also shows the increased tendency for short-circuiting (earlier break-through) associated with increasing gas flow rate.

The early breakthrough seen in Figs. 8 and 9 is due, in part, to upward flow of liquid phase in the bubble plume and reduction of the effective column cross sectional area through which downward-flowing liquid passes. Because the late portions of the *F* curves approach the value 1.0 very slowly, there is significant hold-back or backmixing of the tracer in the reactor. This is likely due to entrainment of the tracer into the bubble plume and transport of the tracer upward in the reactor.

Non-linear regression was used to fit candidate residence time distribution models to the experimentally measured residence distribution curves. The gamma function (an approximation to the solution of the transient *N*-CSTRs in series model) and the inverse Gaussian function (an approximation to the solution of the axial dispersion model) were fit to the data by varying their model parameters. Since both models have two parameters, the best fit model was the model yielding the lowest sum of squares of errors between the model prediction and the experimental data. For all gas flow rates the inverse Gaussian model provided the best fit to experimental data.

The dispersion number was estimated from the variance of the inverse Gaussian distribution using the following equation

$$\nu = 2D - 2D^2(1 - e^{D}) \tag{21}$$

where υ is the dimensionless variance ratio.

Fig. 11 shows dispersion number, *D*, calculated from experimental data (as described above) plotted along with the dispersion number estimates from relations for countercurrent bubble column found in the literature (Table 1) and with estimates made using CFD calculations. The experimental estimates of the dispersion number are shown with a 90% confidence interval. To estimate the dispersion number from CFD calculations, the volume averaged specific turbulence energy dissipation rate, $\bar{\varepsilon}$, was calculated for each gas flow rate and used in the expression proposed by Baird and Rice (1975) to calculate axial dispersion

$$E_L = 0.35 d_c^{4/3} \bar{\varepsilon}^{1/3} \tag{22}$$

The corresponding dispersion number was calculated using Eq. (2).

The dispersion number rises sharply as gas flow increases from 0 to 0.5 L/min, is relatively constant for moderate gas flow rate and rises as gas flow rate increases above 2 L/min. The Kim expression (listed in Table 1) fits experimental data well at low and high gas flow rates. Reith's estimate (listed in Table 1) fits the data at moderate gas flow rate. Baird and Rice's (1975) approximation to Eq. (22) ($\varepsilon = U_G d_c$) consistently overpredicts the dispersion number.

CFD estimates for the dispersion number offer the best match to experimental data, falling within a 90% confidence interval around experimental values at intermediate gas flow rates. Like experimental values, the CFD estimate of the dispersion number does not vary significantly at intermediate gas flow rates. This agreement indicates that the CFD model accounts for the important hydrodynamics in this regime.

Summarizing experimental observations, RTD analyses indicate three flow regimes encountered over the range of gas flows. At low gas flow rate (1 L/min and below) there is very little backmixing and the dispersion number rises sharply with increasing gas flow rate. At intermediate gas flow rates (1.5 L/min $\leqslant Q_{gas} \leqslant$ 2.5 L/min), the dispersion number is relatively con-

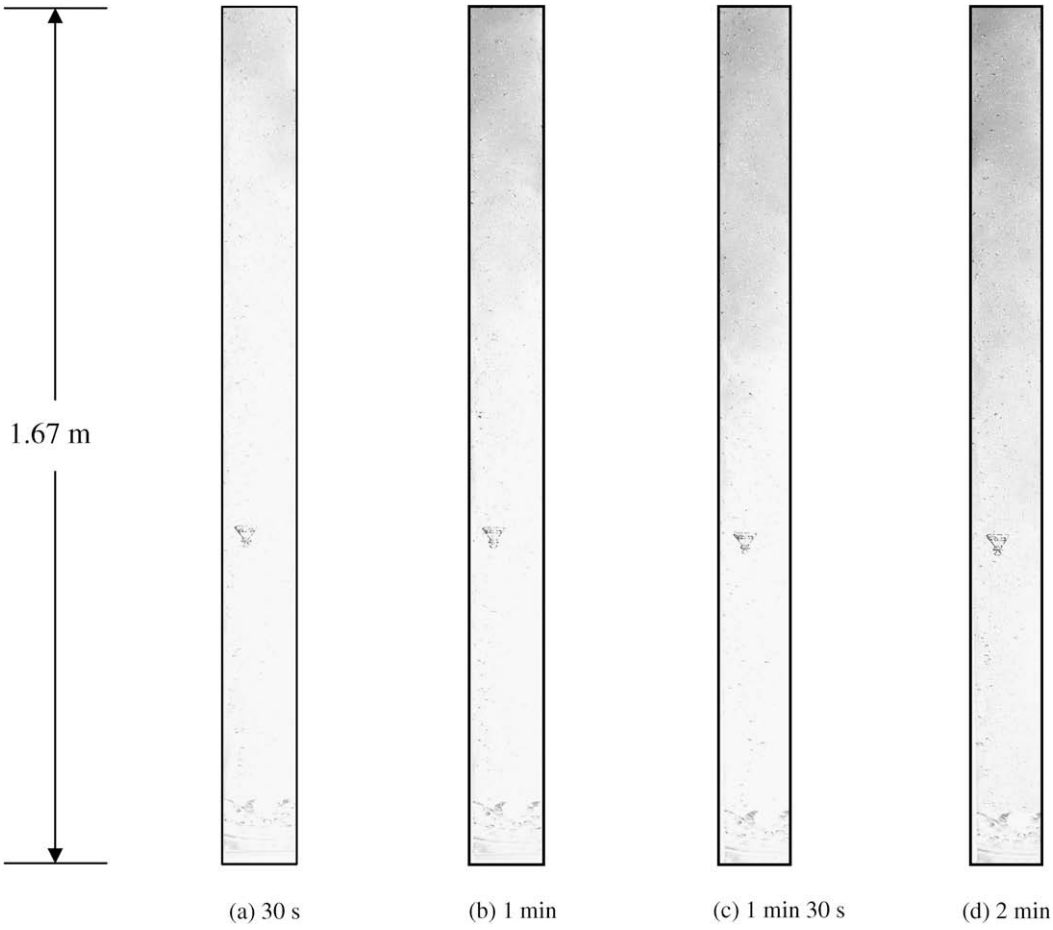

Fig. 7. Experimental flow visualization. Progress of indigo dye tracer in the reactor at 30 s, 1 min, 1 min 30 s and 2 min after introduction of the dye in the reactor feed.

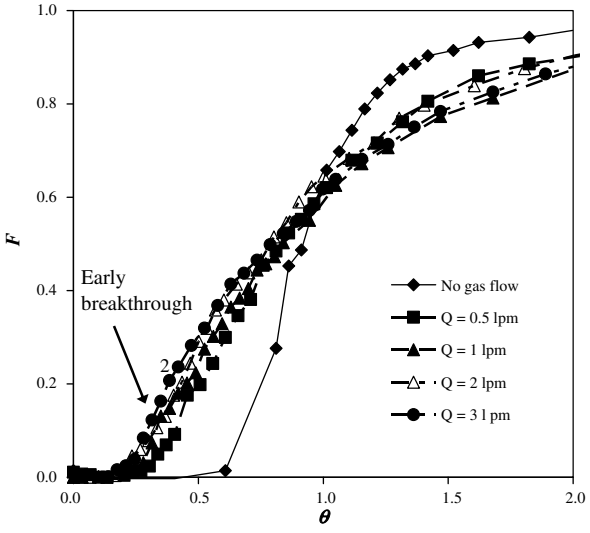

Fig. 8. Experimental tracer curves for liquid flow rate of 6.6 L/min and gas flow rates $0 \leqslant Q_g \leqslant 3$ L/min.

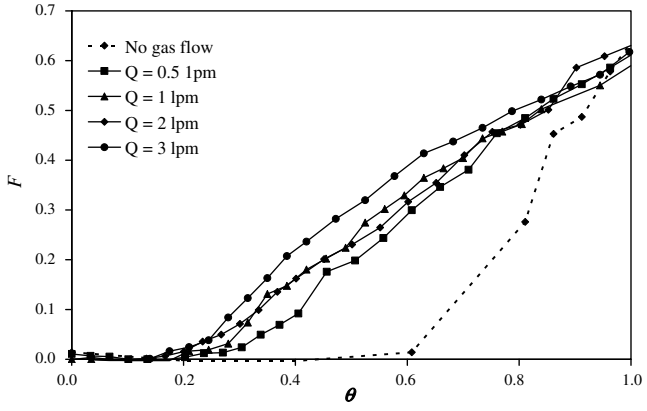

Fig. 9. Tracer data, emphasizing early portion of the tracer curves.

stant. In this regime the bubble plume rises asymmetrically in the column and near the sparger it rotates within the column. At high gas flow rates dispersion number rises slightly and backmixing increases significantly. Churn turbulent behavior (significant bubble break-up and coalescence) was not observed during any experiment.

4.3. Numerical studies

Numerical studies were performed to develop a detailed understanding of the mixing phenomena and trends identified in experimental studies. Specifically, details were sought on the variation in mixing over the axial extent of the reactor. Transient simulations, summarized in Table 2, were performed at a liquid flow rate of 6.6 L/min and gas flow rates ranging from 0.4 to 2.0 L/min. Virtual tracer studies (simulation of step-feed of a conservative tracer) were also performed for single-phase and two-phase flow in the bubble column. For the single-phase virtual tracer study, liquid

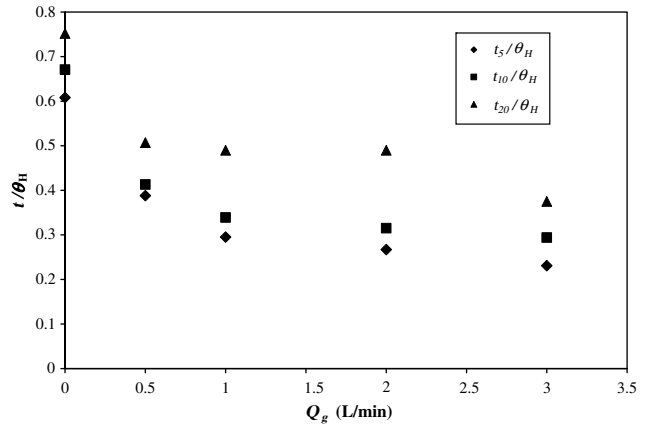

Fig. 10. Variation in t_5/θ_H, t_{10}/θ_H and t_{20}/θ_H with gas flow rate ($0 \leqslant Q_g \leqslant 3$ L/min, $Q_L = 6.6$ L/min).

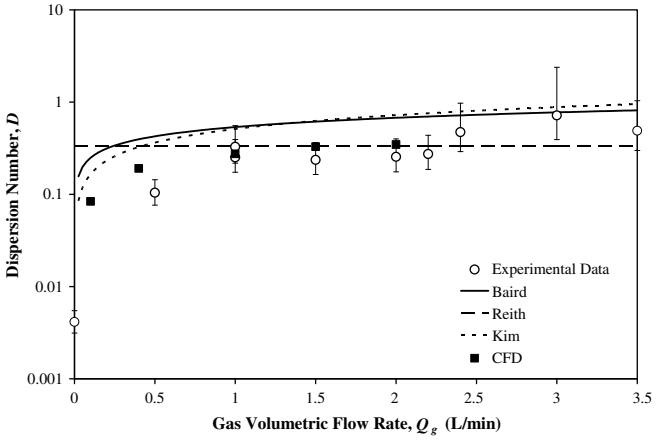

Fig. 11. Experimental and predicted dispersion number, D, as a function of gas flow rate.

flow rate was 6.6 L/min. For the two-phase virtual tracer study, liquid flow rate was 6.6 L/min and gas flow rate was 2.0 L/min. Fig. 12 shows contours of virtual tracer concentration for two-phase operation of the bubble column at 20, 40 and 60 s after introduction of the tracer. Red indicates the tracer concentration is equal to the feed concentration and blue indicates zero tracer concentration. The images in Fig. 12 compare favorably with the experimental flow visualization images found in Fig. 7. As seen in experiments, the CFD model predicts that the tracer projects downward into the reactor along the reactor sides, swirling as it progresses.

Contours of gas volume fraction, ϕ_g, predicted at a gas flow rate of 2 L/min are shown in Fig. 13a. The plume does not rise symmetrically, but migrates in the column and finally migrates to the wall near the top of the column. The plume region, shown in Fig. 13b is defined as the region within which the liquid phase velocity is upward. The surface shown in Fig. 13b is an isosurface where liquid vertical velocity, w_L, is equal to zero. Note that there is upflow of liquid in the bubble plume over the entire reactor height and that the plume twists as it rises in the column. These figures illustrate non-axisymmetric plume rise and significantly different plume shape near the sparger compared with higher locations. In drinking water treatment, asymmetric flow as illustrated in Fig. 13 creates the potential for short-circuiting of raw water and retards ozone mass transfer via poor mixing in the bubble plume and reduced contact of bubbles with raw water. The slight column misalignment introduced into CFD calculations causes the bubble plume to migrate toward the wall and contributes to the non-uniform distribution of phases.

Liquid superficial velocity vectors in the near-sparger region (the bottom 75 cm of the reactor) at four gas flow rates are shown in Fig. 14. At low gas flow rate ($Q_G = 0.4$ L/min) large recirculation regions appear on alternate sides of the plume, causing the plume to rise in a wavy path. When gas flow rate is increased to 1.0 L/min, the bubble plume diameter increases, squeezing the recirculation regions and resulting in faster down-flow of liquid near the column wall. Increasing gas flow rate to 1.5 L/min further increases the velocity of the down-flowing liquid near the column wall. At a gas flow rate of 2.0 L/min, distinct recirculating regions similar to those seen at a gas flow rate of 0.5 L/min appear, though somewhat smaller and with greater rotational speed.

The recirculating regions seen in Fig. 14 explain the plume rise behavior observed during laboratory experiments – these large structures, once established, deflect the bubble plume. These recirculation regions differ from those typically found in bubble column reactors with non-flowing liquid phase. In countercurrent flow, the large scale flow structures move downward with the liquid flow, tending to swirl around the reactor as they proceed. As these fluid structures progress, the bubble plume is deflected, resulting in a chaotic bubble plume motion. The shapes and locations of large fluid structures are strongly dependent on reactor geometry and the interaction between down-flowing liquid and bubble plume is also expected to be influenced by reactor geometry. The boundary between the bubble plume and down-flowing liquid and the preferential flow path for liquid are clearly seen in Fig. 14. This segregation between the phases is an impediment to mass transfer and provides a "Short-circuit" by which some of the liquid phase passes quickly out of the reactor. In disinfection, this short-circuiting provides a path for pathogenic organisms to elude treatment.

Axial variation in mixing in the column is shown in Fig. 15. Neglecting large-scale fluid motion, local mixing intensity is approximately proportional to the square root of the rate of turbulent energy dissipation (Droste, 1997). The distribution of mixing within the column is critically important to spatial variation in mass transfer within the column, as illustrated in Fig. 16, which shows instantaneous distribution of indigo dye in the bubble column when the liquid influent is an indigo dye solution and the influent gas is a mixture of ozone and air. Ozone decolors indigo dye via a rapid reaction that occurs in the liquid phase. When indigo dye is present in excess, because the reaction of dissolved ozone with indigo dye is much faster than the mass transfer rate of ozone from the gas phase to the liquid phase, the disappearance of indigo dye (indicated in Fig. 16 by a change in color) indicates mass transfer of ozone to the liquid phase. A full description of this mass transfer visualization technique is provided elsewhere (Bartrand, 2006).

In Fig. 16, the indigo dye concentration in the top portion of the reactor is relatively uniform until the down-flowing dye solution reaches a location approximately 0.75 m above the top of the diffuser. There, the color rapidly changes from dark blue to a lighter blue. In the bottom 30–40 cm of the column (in the vicinity of the sparger) the indigo dye concentration is relatively uniform, indicating the entire region is well-mixed. This well-mixed region can be understood by examining the distribution of mixing intensities predicted in the reactor by CFD, as shown in Fig. 15b. In the vicinity of the sparger, there is an entrance region for the bubble plume in which mixing is intense and the bubble plume is energetic. In that region the bubble plume is not distributed across the column cross section and the dissolved ozone concentration within the bubble plume is much higher than that in the water surrounding the bubble plume. As fresh (blue) down-flowing water is entrained into the bubble plume, the dye is decolored.

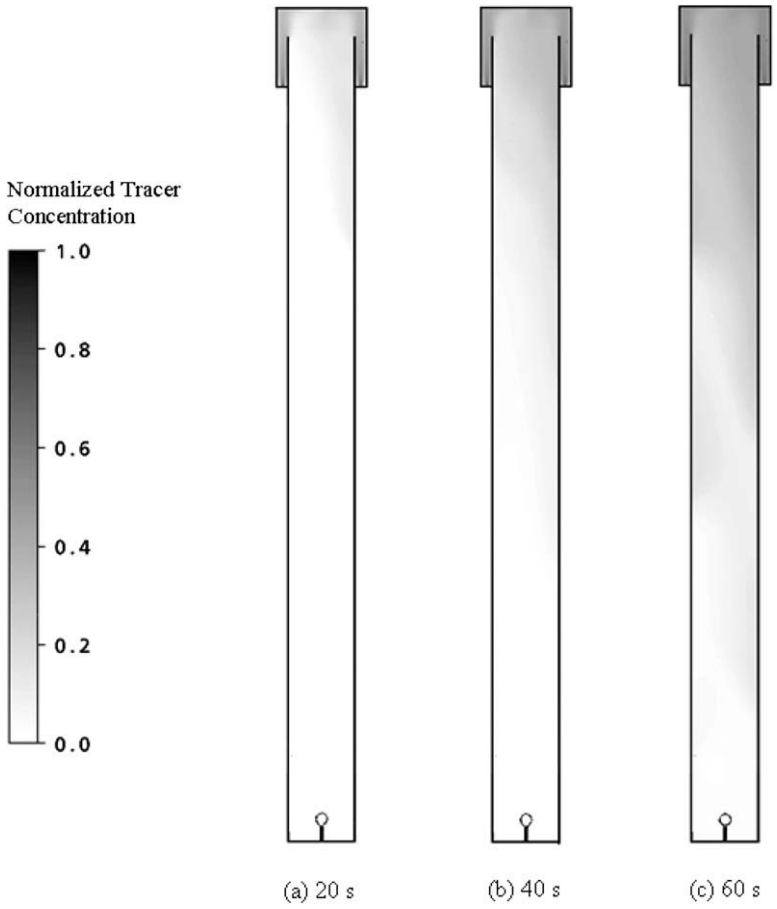

Fig. 12. Computed tracer concentrations at 20, 40 and 60 s after step feed. Liquid and gas flow rates are 6.6 and 2.0 L/min, respectively.

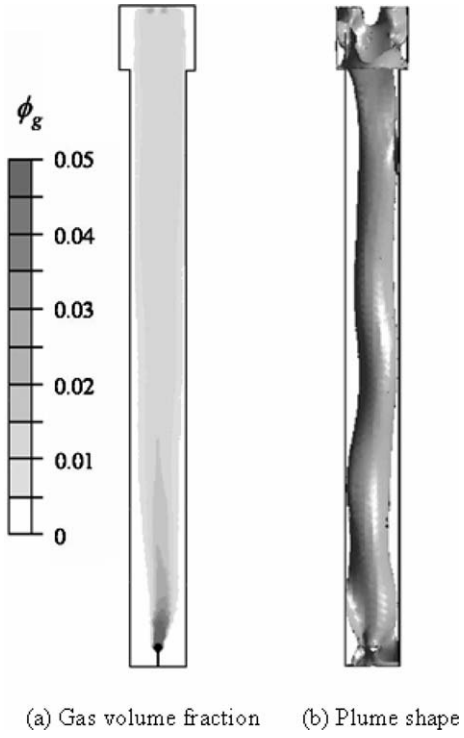

Fig. 13. (a) Contours of predicted gas volume fraction, ϕ_g, at a gas flow rate of 2 L/min and liquid flow rate of 6.6 L/min (b) an isosurface where liquid vertical velocity, w_L, is equal to zero.

Figs. 15 and 16 illustrate the importance of the spatial variation in mixing in the ozone mass transfer process. The non-uniform mixing observed and predicted for the countercurrent pilot bubble column used in the current study are expected to be manifest in full-scale reactors, which will also have entry regions where the gas phase is energetic and mixing is intense.

5. Discussion

Three characteristic hydrodynamic behaviors were observed within ideal bubbly two-phase flow regime in countercurrent flows in a cylindrical bubble column. At low gas to liquid flow ratios the bubble plume rises more or less symmetrically and backmixing in the liquid phase is minimal. At higher gas flow rates the bubble plume does not ascend symmetrically and mixing is not strongly influenced by gas flow rate. At high gas flow rates (at and above 3 L/min), mixing is a strong function of gas flow rate, rising sharply with increasing gas flow rate. These observations indicate that existing mixing and mass transfer models developed for countercurrent flow in cylindrical bubble columns in the ideal bubbly regime may have more limited applicability than has been suggested previously. These findings also indicate the need for systematic studies of mixing in geometries other than right circular cylinders.

CFD analyses and flow visualization studies confirm wide variation in mixing along the axial extent of the reactor, with non-uniformities becoming more pronounced at higher gas flow rates. In general, more vigorous mixing was encountered in the bottom 50 cm of the reactor (near the sparger) than in the rest of the reactor. In water disinfection processes a very high level of inactivation

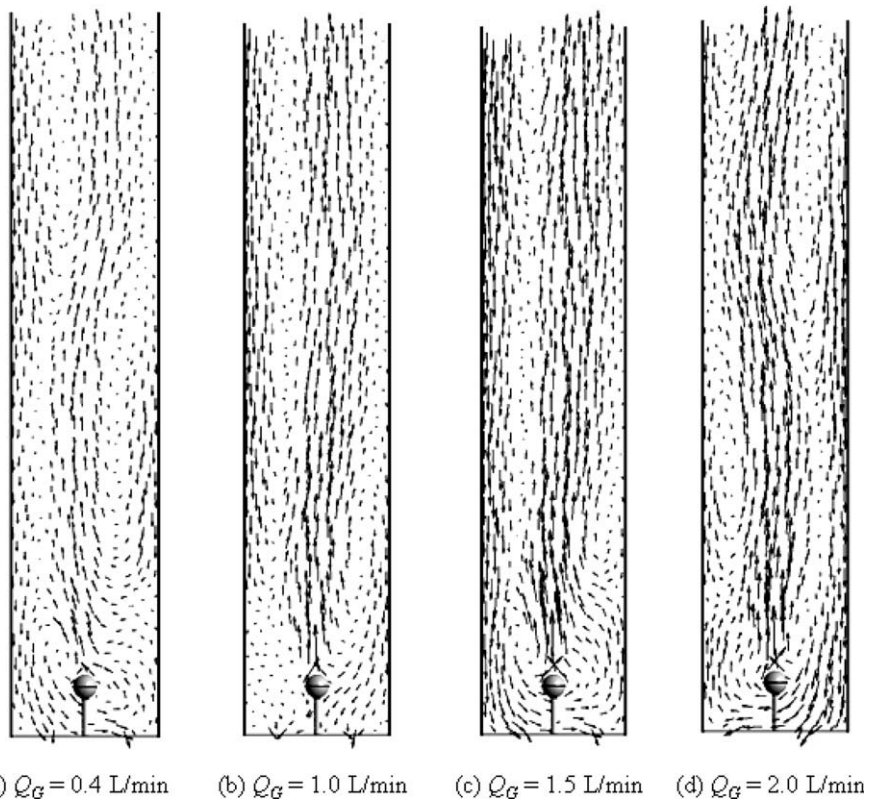

Fig. 14. Predicted water superficial velocity ($\phi_L \vec{V}_L$) field along the vertical midplane. Liquid volumetric flow rate is 6.6 L/min. Gas flow rates are indicated. Vector length indicates magnitude.

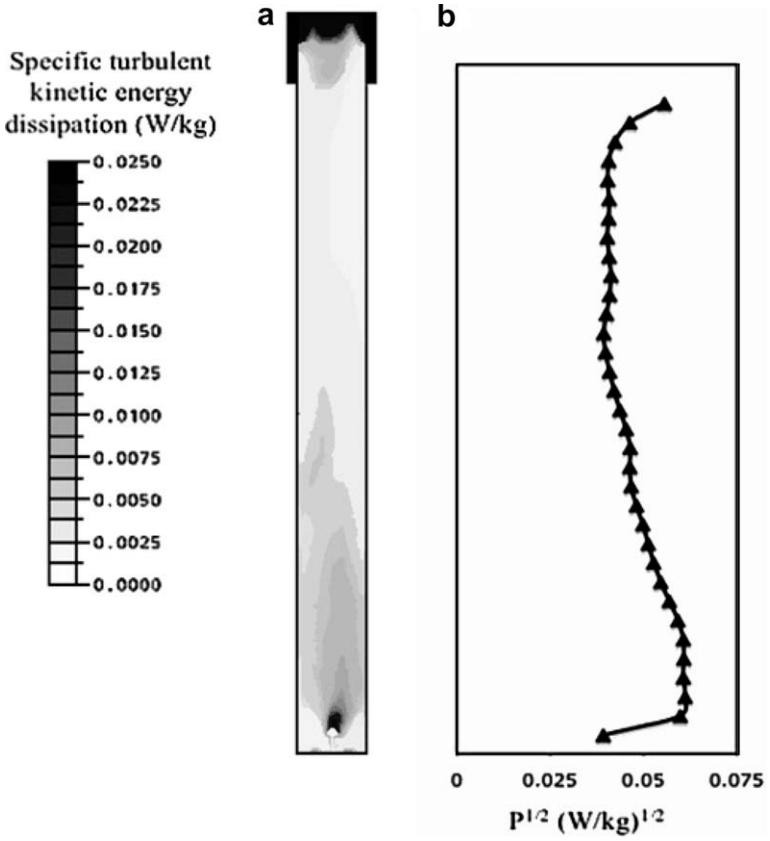

Fig. 15. (a) Contours of dissipation rate of turbulent kinetic energy along a column midplane (b) mean dissipation rate as a function of axial location.

Fig. 16. Indigo dye decoloration by ozone absorbed into the liquid phase. Q_g = 0.4 L/min and Q_L = 6.6 L/min.

of pathogenic organisms may be required. The observed spatial variations in mixing can adversely impact the disinfection efficiency through non-uniform distribution of disinfectant (ozone) and by reducing contact between down-flowing pathogen-laden water and water with high ozone concentration. These findings indicate that dispersion relations for bubble column reactors are specific to the column design and operating conditions. In very tall columns in which the entrance zone of the gas jet is small compared with the overall column height, axial variations in dispersion will be minor, but large-scale hydrodynamics may be different than in smaller reactors.

The numerical model used in the present study was adequate to reproduce significant features in the flowfield and results of CFD studies provided explanation for the unexpectedly early breakthrough of tracer during tracer studies at high gas flow rates. Success of the CFD model in predicting the dispersion number without adjustment or calibration indicates that CFD can be used to supplement pilot studies of bubble columns and may be a better tool for scale-up from pilot to full scale than the relations most commonly used for bubble column reactor scale-up. In particular, since CFD models of mixing, drag and mass transfer are independent of reactor geometry, CFD appears well-suited to analysis of scaled-up reactors with geometries and operating conditions (number of spargers, proximity of spargers to walls, shape of reactor, orientation of gas and liquid streams) differing from those of pilot reactors.

Acknowledgements

The authors acknowledge the support of the L.D. Betz Endowment in Environmental Engineering and the Koerner Family Fellowship at Drexel University for the support of this research. The work of Ms. Kim Digiovanni and Mr. Russell Goodman in data collection is also acknowledged.

References

ANSYS, Inc., 2004. CFX, Canonsburg, PA.
Argo, W.B., Cova, D.R., 1965. Longitudinal mixing in gas-sparged tubular vessels. Ind. Eng. Chem.: Process Des. Dev. 4, 352–359.
Bader, H., Hoigné, J., 1981. Determination of ozone in water by the indigo method. Water Res. 15, 449–456.
Baird, M.H.I., Rice, R.G., 1975. Axial dispersion in large unbaffled columns. Chem. Eng. J. 9, 171–174.
Bartrand, T.A., 2006. High Resolution Experimental Studies and Numerical Analysis of Fine Bubble Ozone Disinfection Contactors, Ph.D. Thesis, Drexel University, Philadelphia.
Bellamy, W.D., Finch, G.R., Haas, C.N., 1998. Integrated Disinfection Design Framework. American Water Works Research Foundation, Denver, CO.
Bischoff, K.B., Phillips, J.B., 1966. Longitudinal mixing in orifice plate gas-liquid reactors. Ind. Eng. Chem. Proc. Dd. 5, 416–421.
Brouckaert, C.J., Buckley, C.A., 1999. The use of computational fluid dynamics for improving the design and operation of water and wastewater treatment plants. Water Sci. Technol. 40, 81–89.
Burrows, L.J., Stokes, A.J., West, J.R., Forster, C.F., Martin, A.D., 1999. Evaluation of different analytical methods for tracer studies in aeration lanes of activated sludge plants. Water Res. 33, 367–374.
Clift, R., Grace, J.R., Weber, M.E., 1978. Bubbles, Drops and Particles. Academic Press, New York, NY.
Cockx, A., Do-Quang, Z., Liné, A., Roustan, M., 1999. Use of computational fluid dynamics for simulating hydrodynamics and mass transfer in industrial ozonation towers. Chem. Eng. Sci. 54, 5085–5090.
Cui, Z., Fan, L.-S., 2004. Turbulence energy distributions in bubbling gas–liquid and gas–liquid–solid flow systems. Chem. Eng. Sci. 59, 1755–1766.
Danckwerts, P.V., 1953. Continuous flow systems distribution of residence times. Chem. Eng. Sci. 2, 13.
Danckwerts, P.V., 1958. The effect of incomplete mixing on homogeneous reactions. Chem. Eng. Sci. 8, 93–102.
Deen, N.G., Solberg, T., Hjertager, B.H., 2001. Large eddy simulation of the gas–liquid flow in a square cross-sectioned bubble column. Chem. Eng. Sci. 56, 6341–6349.
Degaleesan, S., Dudokovic, M., Pan, Y., 2001. Experimental study of gas-induced liquid-flow structures in bubble columns. AIChE J. 47, 1913–1931.
Delnoij, E., Westerweel, J., Deen, N.G., Kuipers, J.A.M., van Swaaij, W.P.M., 1999. Correlation PIV applied to bubble plumes rising in a bubble column. Chem. Eng. Sci. 54, 5159–5171.
Do-Quang, Z., Roustan, M., Duguet, J.-P., 2000. Mathematical modeling of theoretical Cryptosporidium inactivation in full-scale ozonation reactors. Ozone Sci. Eng. 22, 99–111.
Drahos, J., Zahradník, J., Fialová, M., Bradka, F., 1992. Identification and modeling of liquid flow structures in bubble column reactors. Chem. Eng. Sci. 47, 3313–3320.
Droste, R.L., 1997. Theory and Practice of Water and Wastewater Treatment. John Wiley and Sons, New York.
Ducoste, J.J., Carlson, K., Bellamy, W.D., 2001. The integrated disinfection design framework approach to reactor hydraulics characterization. J. Water Supply Res. Technol: AQUA 50, 245–261.
Ekambara, K., Joshi, J.B., 2003. CFD simulation of mixing and dispersion in bubble columns. Trans. Inst. Chem. Eng. 81, 987–1002.
Forret, A., Schweitzer, J.-M., Gauthier, T., Krishna, R., Schweich, D., 2003. Influence of scale on the hydrodynamics of bubble column reactors: an experimental study in columns of 0 1, 0.4 and 1 m diameters. Chem. Eng. Sci. 58, 719–724.
Freire, A.P.S., Miranda, D.D.E., Luz, L.M.S., França, G.F.M., 2002. Bubble plumes and the Coanda effect. Int. J. Multiphase Flow 28, 1293–1310.
Haas, C.N., Joffe, J., Anmangandla, U., Hornberger, J.C., Health, M.S., Jacangelo, J., Glicker, J., 1995. Development and Validation of Rational Design Methods of Disinfection. American Water Works Association Research Foundation, Denver.
Hart, F.L., 1979a. Modifications for the chlorine contact chamber. J. N. Engl. Water Pollut. Control Assoc. 13, 135–151.
Hart, F.L., 1979b. Improved hydraulic performance of chlorine contact chambers. J. Water Pollut. Control Fed. 51, 2868–2875.
Hasan, A.R., Kabir, C.S., Srinivasan, S., 1994. Countercurrent bubble and slug flows in a vertical system. Chem. Eng. Sci. 49, 2567–2574.
Henry, D.J., Freeman, E.M., 1995. Finite element analysis and T_{10} optimization of ozone contactors. Ozone Sci. Eng. 17, 587–606.

Ives, K.J., Hoyer, O., 1998. Tracer studies of the hydraulics of tapered flocculation. Water Sci. Technol. 37, 69–77.
Jakobsen, H.A., 2001. Phase distribution phenomena in two-phase bubble column reactors. Chem. Eng. Sci. 56, 1049–1056.
Joshi, J.B., 2001. Computational flow modelling and design of bubble column reactors. Chem. Eng. Sci. 56, 5893–5933.
Joshi, J.B., Vitankar, V.S., Kulkarni, A.A., Dhorte, M.T., Ekambara, K., 2002. Coherent flow structures in bubble column reactors. Chem. Eng. Sci. 57, 3157–3183.
Kim, J.-H., Tomiak, R.B., Mariñas, B.J., 2002. Inactivation of Cryptosporidium oocysts in a pilot-scale ozone bubble-diffuser contactor. I: Model development. J. Environ. Eng. 128, 514–521.
Krishna, R., Urseanu, M.I., van Baten, J.M., Ellenberger, J., 1999. Influence of scale on the hydrodynamics of bubble columns operating in the churn-turbulent regime: experiments vs. Eulerian simulations. Chem. Eng. Sci. 54, 4903–4911.
Laín, S., Bröder, D., Sommerfeld, M., 1999. Experimental and numerical studies of the hydrodynamics in a bubble column. Chem. Eng. Sci. 54, 4913–4920.
Laín, S., Bröder, D., Sommerfeld, M., 2002. Modeling hydrodynamics and turbulence in a bubble column using the Euler–Lagrange procedure. Int. J. Multiphase Flow 28, 1381–1407.
Langlais, B., Reckhow, D.A., Brink, D.R., 1991. Ozone in Water Treatment: Application and Engineering. Lewis Publishers, Inc., Chelsea, MI.
Levenspiel, O., Smith, W.K., 1957. Notes on the diffusion-type model for the longitudinal mixing of fluids in flow. Chem. Eng. Sci. 6, 227–233.
Lopez de Bertodano, M., Moraga, F.J., Doe, J., 2004. The modeling of lift and dispersion forces in two-fluid simulations of a bubbly jet. J. Fluids Eng. 126, 573–577.
Machina, D.W., McCorquodale, J.A., Bewtra, J.K., 1992. Numerical and physical modeling of air diffuser plume. J. Environ. Eng. 118, 253–267.
Mariñas, B.J., Liang, S., Aieto, E.M., 1993. Modeling hydrodynamics of ozone residual distribution in a pilot-scale ozone bubble-diffuser contactor. J. AWWA 85, 90–99.
Mitra-Majumdar, D., 1997. Transport and Mixing in Gas–Liquid and Gas–Liquid–Solid Flows in Bubble Columns. Dissertation, Drexel University, Philadelphia, PA.
Mitra-Majumdar, D., Farouk, B., Shah, Y.T., 1998. Two- and three-phase flows in bubble columns: numerical predictions and measurements. Ind. Eng. Chem. Res. 37, 2284–2292.
Murrer, J., Gunstead, J., Lo, S., 1995. The development of an ozone contact tank simulation model. Ozone Sci. Eng. 17, 607–617.
Nauman, E.B., Buffham, B.A., 1983. Mixing in Continuous Flow Systems. John Wiley and Sons, New York.
Olmos, E., Gentric, C., Midoux, N., 2003. Numerical description of flow regime transition in bubble column reactors by a multiple gas phase model. Chem. Eng. Sci. 58, 2113–2121.
Owens, J.H., Miltner, R.J., Rice, E.W., Johnson, C.H., Dahling, D.R., Schaefer III, F.W., Shukairy, H.M., 2000. Pilot-scale ozone inactivation of Cryptosporidium and other microorganisms in natural water. Ozone Sci. Eng. 22, 501–517.
Pan, Y., Dudukovic, M.P., Chang, M., 2000. Numerical investigation of gas-driven flow in 2-D bubble columns. AIChE J. 46, 434–449.
Peplinski, D.K., Ducoste, J.J., 2002. Modeling of disinfection contactor hydraulics under uncertainty. J. Environ. Eng. 128, 1056–1067.
Pfleger, D., Gomes, S., Gilbert, N., Wagner, H.-G., 1999. Hydrodynamic simulations of laboratory scale bubble columns fundamental studies of the Eulerian–Eulerian modeling approach. Chem. Eng. Sci. 54, 5091–5099.
Rakness, K.L., Stover, E.L., Krenek, D.L., 1984. Design, start-up and operation of an ozone disinfection unit. J. Water Pollut. Control Fed. 56, 1152–1159.
Rasband, W.S., 2007. ImageJ, U.S. National Institutes of Health, Bethesda, Maryland, USA. Available from: <http://rsb.info.nih.gov/ij/>.
Reith, T., Renken, S., Israël, B.A., 1968. Gas hold-up and axial mixing in the fluid phase of bubble columns. Chem. Eng. Sci. 23, 619–629.
Rice, G.R., Littlefield, M.A., 1987. Dispersion coefficients for ideal bubbly flow in truly vertical bubble columns. Chem. Eng. Sci. 42, 2045–2053.
Ruzicka, M.C., Zahradník, J., Drahos, J., Thomas, N.H., 2001. Homogeneous–heterogeneous regime transition in bubble columns. Chem. Eng. Sci. 56, 4609–4626.
Sanada, T., Watanabe, M., Doe, J., 2005. Behaviour of a single coherent gas bubble chain and surrounding liquid jet flow structure. Chem. Eng. Sci. 60, 4886–4900.
Santoro, D., Bartrand, T.A., Farouk, B., 2005. Use of VFD for wastewater disinfection process analysis: *E. coli* inactivation with peroxyacetic acid. Int. J. Chem. Reactor Eng. 3, A46.
Sanyal, J., Vásquez, S., Roy, S., Dudukovic, M.P., 1999. Numerical simulation of gas–liquid dynamics in cylindrical bubble column reactors. Chem. Eng. Sci. 54, 5071–5083.
Sato, Y., Sekoguchi, K., 1975. Liquid velocity distribution in two-phase bubble flow. Int. J. Multiphase Flow 2, 79–95.
Sawyer, C.M., King, P.H., 1969. The Hydraulic Performance of Chlorine Contact Tanks. 24th Purdue Industrial Waste Conference, Purdue University, W. Lafayette, IN, pp. 1151–1168.
Schmid, B.H., Hengl, M.A., Stephan, U., 2004. Salt tracer experiments in constructed wetland ponds with emergent vegetation: laboratory study on the formation of density layers and its influence on breakthrough curve analysis. Water Res. 38, 2095–2102.
Sepp, E., 1981. Optimization of chlorine disinfection efficiency. J. Environ. Div., Proc. ASCE 107, 139–153.
Ta, C.T., Hague, J., 2004. A two-phase computational fluid dynamics model for ozonetank design and troubleshooting in water treatment. Ozone Sci. Eng. 26, 403–411.
Tang, G., Adu-Sarkodie, K., Kim, D., Kim, J.-H., Teefy, S., Shukairy, H.M., Mariñas, B., 2005. Modeling *Cryptosporidium parvum* oocyst inactivation and bromate formation in a full-scale ozone contactor. Environ. Sci. Technol. 39, 9343–9350.
Teefy, S.M., Singer, P.C., 1990. Performance analysis of tracer tests to determine compliance of a disinfection scheme with the SWTR. Am. Water Works Assoc. J..
van Baten, J.M., Krishna, R., 2001. Eulerian simulation for determination of the axial dispersion of liquid and gas phases in bubble columns operating in the churn turbulent regime. Chem. Eng. Sci. 56, 503–512.
von Gunten, U., 2003. Ozonation of drinking water: Part 1. Oxidation kinetics and product formation. Water Res. 37, 1443–1467.
Zahradník, J., Fialová, M., 1996. The effect of bubbling regime on gas and liquid phase mixing in bubble column reactors. Chem. Eng. Sci. 51, 2491–2500.